

A Neural Surrogate-Enhanced Multi-Method Framework for Robust Wing Design Optimization

Arash Fath Lipaei * †

Graduate Student, Istanbul, Istanbul, 34450, Turkey

AmirHossein Ghaemi ‡

Independent Researcher

Melika Sabzikari §

Graduate, London, Greater London, SW7 2AZ, United Kingdom

This paper introduces a modular and scalable design optimization framework for the wing design process that enables faster early-phase design while ensuring aerodynamic stability. The pipeline starts with the generation of initial wing geometries and then proceeds to optimize the wing using several algorithms. Aerodynamic performance is assessed using a Vortex Lattice Method (VLM) applied to a carefully selected dataset of wing configurations. These results are employed to develop surrogate neural network models, which can predict lift and drag rapidly and accurately. The stability evaluation is implemented by setting the control surfaces and components to fixed positions in order to have realistic flight dynamics. The approach unifies and compares several optimization techniques, including Particle Swarm Optimization (PSO), Genetic Algorithms (GA), gradient-based MultiStart methods, Bayesian optimization, and Lipschitz optimization. Each method ensures constraint management via adaptive strategies and penalty functions, where the targets for lift and design feasibility are enforced. The progression of aerodynamic characteristics and geometries over the optimization iterations will be investigated in order to clarify each algorithm's convergence characteristics and performance efficiency. Our results show improvement in aerodynamic qualities and robust stability properties, offering a mechanism for wing design at speed and precision. In the interest of reproducibility and community development, the complete implementation is publicly available on **GitHub**.

*Corresponding author: alipaei25@edu.ku.tr, All authors contributed equally.

†Graduate Student, Graduate School of Sciences and Engineering, Koç University, Rumelifeneri Yolu, Sarıyer, Istanbul, Istanbul, Turkey.

‡Independent Researcher.

§Graduate, Faculty of Mechanical Engineering, Imperial College London, Exhibition Road, London, Greater London, United Kingdom.

I. Introduction

The efficient design of aircraft wings has become a significant challenge in aerospace engineering, particularly during the initial phases of glider design, where iterations must be rapid and analysis must be cost-effective. Typical design cycles employ computational fluid dynamics (CFD), which, although accurate, is also computationally prohibitive and often unusable for broader design space exploration. Recent works have explored methods using surrogate models as well as optimization techniques, in order to reduce design cycle duration while keeping fidelity. In this paper, a Combined Hybrid Intelligent Multimethod Ensemble for Robust Aero-wing Optimization is proposed as a scalable framework that combines physics-based simulations, machine learning surrogates, and multiple optimization methods. The proposed solution offers a timely and reliable approach to exploring wing configurations that are able to balance aerodynamic performance and flight stability, and thus offers a practical and rapid approach to the modern context of wing development.

A. Background and Related Work

Wing design for glider aircraft requires a careful balance of aerodynamic efficiency and stability, all under strict structural and operational constraints. As the design complexity increases, the need for plausibly safe and effective computational tools becomes even more valuable for high-dimensional parameter domains. Classical optimization methods, which rely heavily on high-fidelity simulations, like CFD, have issues scaling due to their computational cost, time, and resource requirements. Heuristic methods provide flexibility; however, they do not have guarantees of accuracy or convergence. New advancements in surrogate modeling, machine learning, and hybrid optimization methods present potential for closing this gap.

Adjoint-based approaches continue to play a significant role in aerodynamic shape optimization, as these approaches can reliably compute the gradient with respect to many design variables at a relatively low cost, and recent research has implemented stability constraints in the optimization process [1]. To reduce the reliance on adjoint solvers, adjoint-free methods have been developed for complex geometries and configurations, such as the Common Research Model wing, that achieved similar fidelity without having to solve adjoint equations [2]. Surrogate-assisted adjoint techniques have also been explored, for example, by integrating radial basis functions such that they converge more effectively [3]. Gradient prediction techniques based on dynamic-mode decomposition have lessened the computational time for gradient solutions by more than 80%, and thus accelerated the computation [4]. Unified adjoint formulations for lattice Boltzmann methods have broadened the applicability to viscous/inviscid, compressible/incompressible, and 2D/3D flows [5]. Robust design regulations have been integrated into adjoint frameworks by coupling uncertainty quantification via polynomial chaos expansion, as a way to obtain designs that optimized aerodynamic performance while yielding robustness under multiple uncertainty sources [6].

In parallel, deep learning and surrogate modeling are providing new alternatives to aerodynamic design. Neural-

network surrogates that are integrated with gradient-based optimization improve convergence speed and the quality of the solutions [7], while data-driven techniques provide efficient exploration of large wing design spaces [8]. The applications are extending from turbo-machinery [9], generative modeling of unconventional and non-standard configurations [10, 11], and hybrid methods integrating genetic algorithms and deep neural networks for airfoil optimization [12]. Adaptive machine learning-based methods have allowed for optimization of finite wings for different sets of flight conditions [13], whereas deep learning techniques have managed to outperform reduced-order methods in more complex non-linear transonic regimes [14]. Geometric filtering methods provide further constraints on design spaces on physically valid yet aerodynamically innovative shapes [15].

Multi-fidelity and transfer-learning approaches have been extensively implemented for balancing accuracy and computational efficiency. For instance, CNN-based multi-fidelity surrogates [16, 17], surrogate-assisted optimization of aircraft wings [18], and transfer-learning frameworks aimed at the transfer of aerodynamic knowledge across modeling problems [19]. The inverse design approaches that combine multi-fidelity simulations with machine learning have extended the applicability as well [20]. Component-level studies, such as minimizing wing–fuselage interference, further highlight the value of multi-fidelity and hybrid optimization approaches [21].

There has been a growing focus on multi-objective optimization, uncertainty quantification, and robustness. New contributions include efficient handling of geometric constraints [22], improved global search strategies for expensive problems [23], multi-objective particle swarm optimization methods tailored to turbo-machinery [24], and the use of deep-learning-aided evolutionary algorithms to produce the Pareto front [25]. Many robust optimization approaches contain uncertainty quantification by implementing radial basis function (RBF) surrogates [26], stochastic gradient-based optimization [27], as well as uncertainty-aware surrogates for complex aerodynamic problems. Off-design performance analysis is derived from imposed constraints that accurately emulate real-world flight environments while requiring very few simulations [28].

In addition to conventional aircraft, novel optimization methods have also been implemented for unconventional and biologically inspired configurations. The triangular airfoils for Martian flight [29], corrugated wing designs refined with reinforcement learning [30], Unmanned Aerial Vehicle (UAV) penetration strategies with six degrees of freedom using deep reinforcement learning [31], and aero-structural systems that balance weight and stiffness for high-aspect-ratio wings [32], are all few of the studies implementing novel optimization methods. Hybrid surrogate–metaheuristic methods were also employed in lightweight structural designs for flexible wings [33].

There are still persisting fundamental difficulties with respect to sensitivity to initial conditions, representation of geometry, and robustness to uncertainty. There has been research around conducting statistical analysis of optimization robustness [34], dynamically controlling geometry to maintain quality of the mesh [35], compact modal design variable parameterizations [36], and optimization using a large database of design variables [37]. Distributionally robust formulations have further improved resiliency to uncertain data [38]. Reviews have detailed the continuing challenges

in balancing fidelity, cost, and multidisciplinary complexity [39].

Lastly, recent works have associated mission-level objectives with aerodynamic design. [40] Reinforcement learning with long short-term memories (LSTMs) was used in UAVs, in order to optimize communication under energy constraints [40]. In the configuration level, machine learning-based optimization has also helped accelerate the design of unconventional configurations such as the box wings, demonstrating meaningful efficiency gains that were validated with Reynolds-Averaged Navier–Stokes equations (RANS) [41]. Overall, these advancements suggest a shift towards combining surrogates, physics-based models, and intelligent algorithms into a unified, scalable framework.

B. Contribution of This Work

This work presents CHIMERA (Combined Hybrid Intelligent Multimethod Ensemble for Robust Aero-wing Optimization), an innovative optimization framework that utilizes physics-based simulation, surrogate modeling, and a multi-method optimization ensemble for the optimization of aero-wing design. In contrast to past methods that emphasize either aerodynamic performance or optimization flexibility as a standalone dimension, CHIMERA leverages both within a manageable pipeline. Contributions include:

- The formulation of a constrained nonlinear optimization problem tailored to glider wing design with aerodynamic constraints.
- The development of dual neural network surrogates—one for continuous aerodynamic prediction and another for binary stability classification—trained on data generated via Vortex Lattice Method simulations and linearization of equations of motion.
- The implementation and comparison of five distinct optimization strategies, each embedded with adaptive constraint handling to ensure design feasibility and lift compliance.
- A comprehensive performance evaluation across algorithms, highlighting convergence behavior, aerodynamic gains, and robustness to initial conditions.
- The public release of the full implementation to encourage reproducibility and further research in hybrid intelligent optimization for aerospace applications.

II. Problem Statement

The process of wing design for glider aircraft involves achieving the best aerodynamic performance while satisfying the physical feasibility constraints. The design process is inherently multi-objective and requires making trade-offs between lift generation and drag minimization. In order to rapidly evaluate candidate designs, the task was posed as a constrained optimization problem, incorporating surrogate models trained on high-fidelity aerodynamic simulations. In this section, we formally define the optimization problem, indicate the design variables and constraints, specify the aerodynamic requirements, and describe the governing mathematical framework.

A. Optimization Problem and Governing Equations

The optimization objective is to identify wing configurations that optimize the aerodynamic performance efficiency, while satisfying flight constraints. More specifically, the design will attempt to minimize the aerodynamic drag during steady gliding flight while generating lift equal to the weight of the glider.

The design vector $\mathbf{x} \in \mathbb{R}^8$ contains eight continuous variables:

$$\mathbf{x} = [c_r, \alpha, \Lambda, b, \theta, \lambda, \Gamma, V], \quad (1)$$

where c_r is root chord, α is angle of attack, Λ is sweep angle, b is wingspan, θ is twist angle, λ is taper ratio, Γ is dihedral angle, and V is flight velocity. These variables define both geometric and operational properties of the wing.

The optimization objective is to minimize drag while maintaining lift constraints. Therefore, it was formulated as a constrained nonlinear program:

$$\min_{\mathbf{x}} f(\mathbf{x}) = \left(\frac{D(\mathbf{x})}{D_0} \right)^2 + \mu \left(\frac{L_{\text{target}}}{L(\mathbf{x})} - 1 \right)^2 \quad (2)$$

$$\text{subject to } \mathbf{x}_{\text{lb}} \leq \mathbf{x} \leq \mathbf{x}_{\text{ub}}, \quad (3)$$

where $L(\mathbf{x})$ and $D(\mathbf{x})$ are lift and drag predicted by a surrogate model, L_{target} is the required lift to balance the glider's weight, D_0 is a normalization constant, and μ is a penalty parameter to enforce the lift requirement.

The surrogate mappings are defined as

$$[L(\mathbf{x}), D(\mathbf{x})] = \mathcal{F}_{\text{aero}}(\mathbf{x}), \quad \mathbf{S}(\mathbf{x}) = \mathcal{F}_{\text{stab}}(\mathbf{x}), \quad (4)$$

with $\mathcal{F}_{\text{aero}}$ representing the aerodynamic predictor and $\mathcal{F}_{\text{stab}}$ denoting the stability classifier.

This formulation supports both global and local optimization algorithms.

B. Design Parameters and Requirements

The optimization problem for the eight variables in \mathbf{x} , constructed based on their impact on aerodynamic behavior, as well as their utility in configurations of gliders. The parameters describe important geometric and operational features, including the planform shapes, the spanwise distribution, and flight conditions.

Aerodynamic performance is represented by two main criteria: (1) Lift is equal to the weight of the glider so that the level flight can be sustained, and (2) drag is minimized to obtain the maximum glide efficiency. These output variables are predicted by a neural network surrogate trained on simulation data generated using a Vortex Lattice Method (VLM), to facilitate fast predictions and evaluation within the optimization loop.

In addition to being aerodynamically feasible, design candidates were also assessed for stability. Stability was evaluated using a second surrogate trained to classify the flight behaviors across ten dynamic derivatives, and across two longitudinal and lateral-directional modes, e.g. roll, pitch, and yaw.

III. Solution Approach

In order to address the challenges of designing a robust and efficient wing, we begin the process by performing physics-based simulations using the vortex lattice method (VLM) in order to create a dataset of wing configurations. We then train surrogate models to approximate the results of the simulations, enabling rapid evaluation during optimization. Multiple optimization algorithms, capable of supporting both local refinement and global exploration, were incorporated in this study.

A. Pipeline for Aerodynamic and Stability Modeling

CHIMERA automates an entire workflow of wing design optimization, from data generation to optimization. Eight (8) parametric variables define the design space, and a representative wing configuration dataset is created with the vortex lattice method (VLM) solver. The solver models steady, incompressible, potential flow around lifting surfaces to generate typically efficient and reasonably accurate estimates for lift distribution, induced drag, and aerodynamic moments. Each configuration is evaluated in steady, level gliding conditions to capture the aerodynamic behavior.

In parallel, the solver calculates stability derivatives for each design, extracting ten total dynamic stability derivatives across longitudinal and lateral-directional modes (i.e., roll, pitch, yaw). This ensures that both aerodynamic performance and flight dynamics are included in the dataset.

From these simulations, two neural network surrogates are trained:

- An **aerodynamic surrogate** for continuous prediction of lift, drag, and moment coefficients.
- A **stability surrogate** that classifies designs as stable or unstable based on dynamic derivatives.

These models replace costly simulation calls during optimization, allowing for quicker iteration of the design space. They are embedded into a common optimization framework that utilizes penalty functions and stability checks to enforce constraints on the design. This setup ensures consistency across each optimization run, enabling comparative studies between different algorithm design approaches, while providing adaptability to new design scenarios.

B. Multi-Method Optimization Strategy

In order to navigate the complex, non-linear design space, CHIMERA supports several optimization algorithms, each representing a complement of exploration and exploitation capabilities:

- **Gradient-Based Optimization (MultiStart)**: Performs local searches from multiple initial points to reduce the risk of trapping in local minima and then applies gradient-based optimization with respective constraints.

- **Genetic Algorithms (GA):** A global, population-based method inspired by natural selection, effective for exploring diverse regions of the design space.
- **Particle Swarm Optimization (PSO):** A swarm-based search that balances exploration of new regions with exploitation of known good solutions.
- **Bayesian Optimization:** A probabilistic, surrogate-assisted approach guided by acquisition functions for efficient global exploration.
- **Lipschitz - Gradient Optimization:** Lipschitz optimization combined with gradients to prune unpromising regions and adaptively refine promising areas.

Every algorithm utilizes the surrogate models and applies the same constraint-handling procedures, allowing for direct and consistent comparisons. For the detailed mathematical formulations of these algorithms, see B. This ensemble approach provides robustness against local minima, accelerates convergence, and allows for a custom optimization process for the complexity of the problem.

IV. Results and Analysis

This section provides a thorough evaluation of the proposed framework, detailing the particulars, performance coverage, and comparisons. First, we will discuss the numerical setup, including that of the data generation, pre-processing, scaling, and the actual hyperparameters and stopping criteria used, so the results are completely reproducible. Next, we will discuss the training and validation of the two neural networks (aerodynamic regression and stability classification) together, along with dataset splits, metrics, calibration, and generalization. With these surrogates fixed, we will showcase the optimized wing designs generated from representative operational conditions and constraints. Next, we provided a sensitivity study that considers the multiple initializations to evaluate the robustness and the attraction basin. Following, we quantify the aerodynamic performance and stability outcomes (i.e., lift, drag, CL , CD , and stability labels) and how we provide uncertainty estimates and agreement with numerical solutions. Trends that we summarized are the design-variable trade-offs, constraint activity, and the role of the trained surrogates. Finally, we concluded this section with the comparisons of the algorithms, highlighting their convergence behavior and sample efficiency, as well as the solution quality of all the optimization strategies.

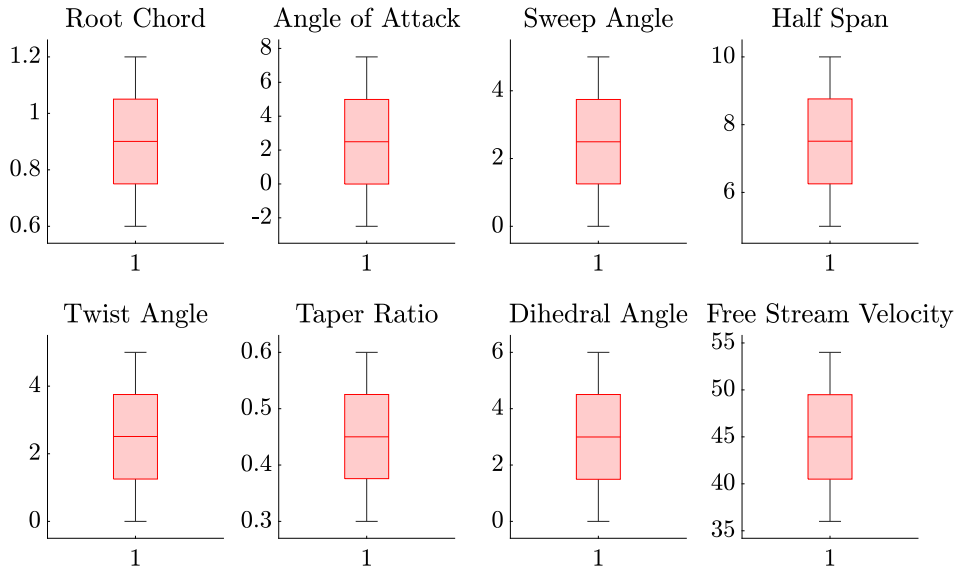
A. Implementation Details

Aerodynamic data were created using a vortex-lattice based solver [42] and stability derivatives were calculated by linearizing the equations of motion about trimmed flight states (derivations shown in A). The input design variables included eight wing and flight parameters: root chord, angle of attack, sweep angle, half-span, twist angle, taper ratio, dihedral angle, and free-stream velocity. Their ranges, listed in Table 1, were selected to allow enough coverage of realistic ultralight aircraft configurations.

Table 1 Design variables and their lower/upper bounds used for dataset generation.

Variable	Lower Bound	Upper Bound
Root chord [m]	0.6	1.2
Angle of attack [deg]	-2.5	7.5
Sweep angle [deg]	0.0	5.0
Half-span [m]	5.0	10.0
Twist angle [deg]	0.0	5.0
Taper ratio	0.3	0.6
Dihedral angle [deg]	0.0	6.0
Velocity [m/s]	36.0	54.0

Before training, the raw dataset, which contained 150,000 sets of data obtained by running the VLM and stability combined simulations on a high-performance computing cluster, was pre-processed by applying an anomaly detection method, implementing the Local Outlier Factor (LOF) algorithm at a contamination level of 0.01% and $k = 200$ neighbors. Next, the features associated with the symmetric flight condition (zero-valued) were removed to speed up training and increase efficiency. All the remaining inputs were normalized to the interval of $[-2, +2]$ to satisfy the scaling requirements of the neural networks. The design variable distributions after sampling are depicted in Figure 1. The box plots indicate that the variables are uniformly distributed within the respective bounds without significant skewness or outliers. This suggests that the surrogate models are trained with a balanced dataset.

**Fig. 1 Box plots of the input design variables showing coverage and distribution within the prescribed bounds.**

The overall workflow of data generation, filtering, and model training is summarized in Figure 2.

The aerodynamic analysis performed in this study utilized a NACA 2412 airfoil throughout the entire span and

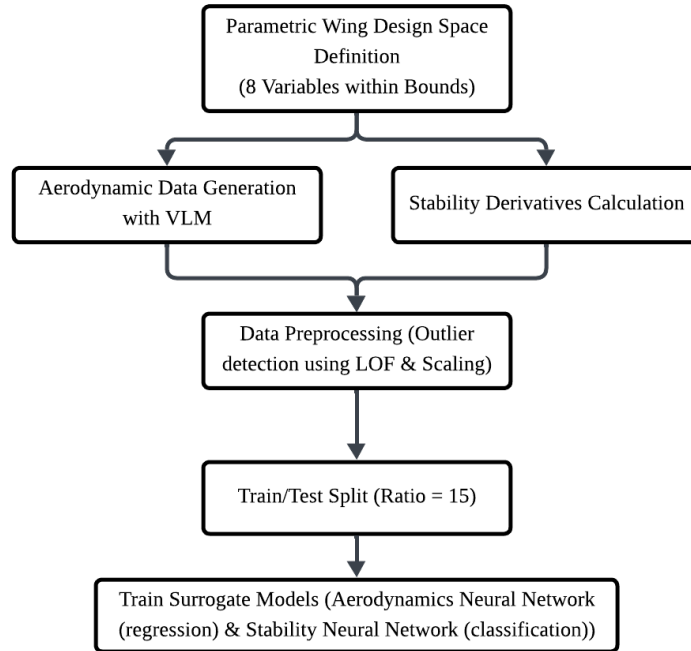


Fig. 2 Workflow of dataset generation, preprocessing, and surrogate model training.

was discretized into 20×40 chordwise and spanwise panels to achieve high-resolution predictions of aerodynamic loading. The airfoil configuration is provided in Fig. 3. Batch simulations were computed at a fixed altitude of 1200 m under the International Standard Atmosphere (ISA). The stability derivatives were calculated in a consistent manner, maintaining the same flow and geometric assumptions. The fixed fuselage and tail dimensions used for all runs, given in Table 2, were held to provide each wing configuration a reasonable assessment within an overall aircraft model. The values assigned to the fixed components of the aircraft in the mentioned table were chosen to represent a conventional ultralight glider design.

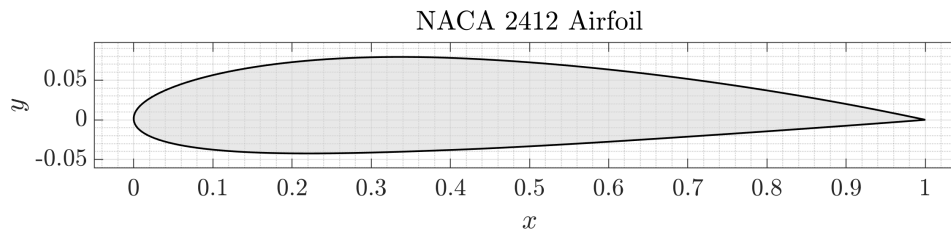


Fig. 3 Airfoil geometry (NACA 2412) used across the span.

These implementation details set up the ability to train credible surrogate models and perform constrained optimizations.

Table 2 Fixed aircraft geometry and mass parameters used for stability analysis.

Parameter	Value
Fuselage length [m]	6.00
Fuselage diameter [m]	0.50
Horizontal tail root chord [m]	1.95
Horizontal tail tip chord [m]	0.60
Horizontal tail span [m]	1.00
Vertical tail root chord [m]	1.95
Vertical tail tip chord [m]	1.00
Vertical tail span [m]	1.30
Wing position along fuselage x [m]	1.75
Wing position along fuselage z [m]	1.90
Horizontal tail position along fuselage x [m]	4.05
Horizontal tail position along fuselage z [m]	1.90
Vertical tail position along fuselage x [m]	4.05
Vertical tail position along fuselage z [m]	1.90
Fuselage mass per unit length [kg/m]	1.00
Tail mass per unit area [kg/m ²]	10.00

B. Neural Network Training and Validation

Two neural networks were created to act as surrogates for aerodynamic and stability predictions. Both implemented a Multi-Layer Perceptron (MLP) with ten hidden layers, with each hidden layer consisting of 512 neurons, residual connections between layers, and ReLU activation functions. This deep architecture allowed the networks to capture the complex nonlinear mapping between the wing geometry, flight parameters, and aerodynamic responses. A diagram of the architectures is presented in Figure 4, where the aerodynamics network and stability/control network share the same architecture but utilize differing loss equations.

The Aerodynamics Prediction Network was developed as a regression network. It was trained using a mean squared error (MSE) loss function to predict continuous outputs such as lift, drag, etc. A few of the important output variables of this network are listed in Table 3. The network structure is shown in Figure 5.

Table 3 Some of the important outputs of the Aerodynamics neural network.

Parameters
C_L
C_D
Lift (L)
Drag (D)

The Control and Stability Prediction Network implemented a similar architecture, although it was structured as a classification problem with three outputs: stable, unstable, or semi-stable. To deploy the network, a cross-entropy

loss function was selected. The network was trained to classify stability across ten derivatives, which represented longitudinal, lateral, and directional modes. The stability parameters assessed by the network are presented in Table 4. Figure 6 demonstrates the prediction workflow for the stability and control network.

Table 4 Outputs of the Control and Stability neural network.

Parameters
F_{XU} stability
M_U stability
F_{YV} stability
F_{ZW} stability
M_α stability
L_β stability
N_β stability
L_P stability
M_Q stability
N_R stability

The training and validation performance of both networks is summarized in Table 5. The Aerodynamics network achieved an average test loss of 2.7% with a kernel regularizer of 0.005, while the Control and Stability network reached an average test loss of 13.7% with a kernel regularizer of 0.001. The test vs train loss for both models shows that the networks are not overfitting.

Table 5 Train-test loss of the neural networks.

Neural Network	Kernel Regularizer	Train Loss	Average Test Loss
Aerodynamics	0.005	0.4%	2.7%
Control & Stability	0.001	14%	13.7%

Overall, the surrogate models demonstrated sufficient accuracy for use in the optimization loop.

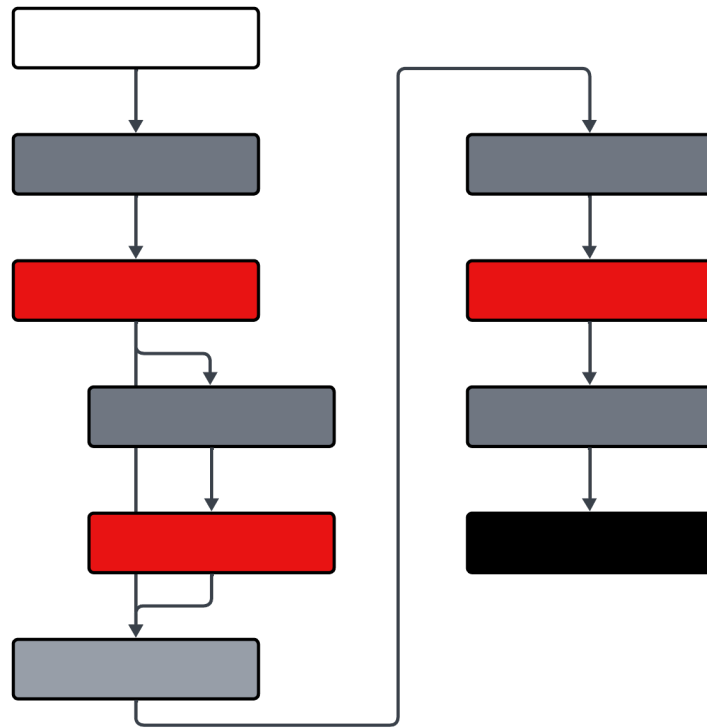


Fig. 4 Architecture of both neural networks (White: Input layer, Dark Grey: Fully connected layer, Red: ReLU activation, Light Grey: Add layer, Black: Output layer). Residual connections exist between hidden layers. (2.4 million trainable parameters).

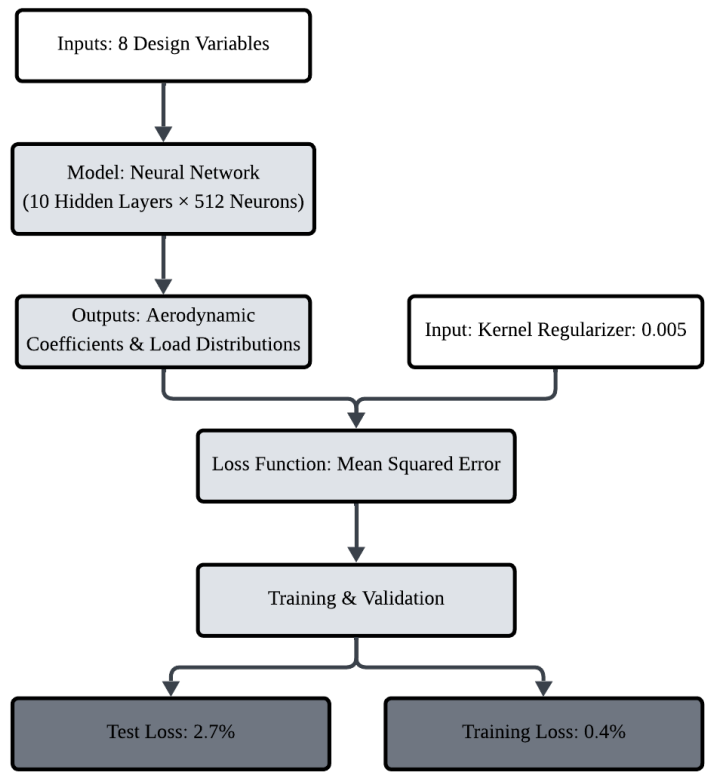


Fig. 5 Aerodynamics Neural Network process.

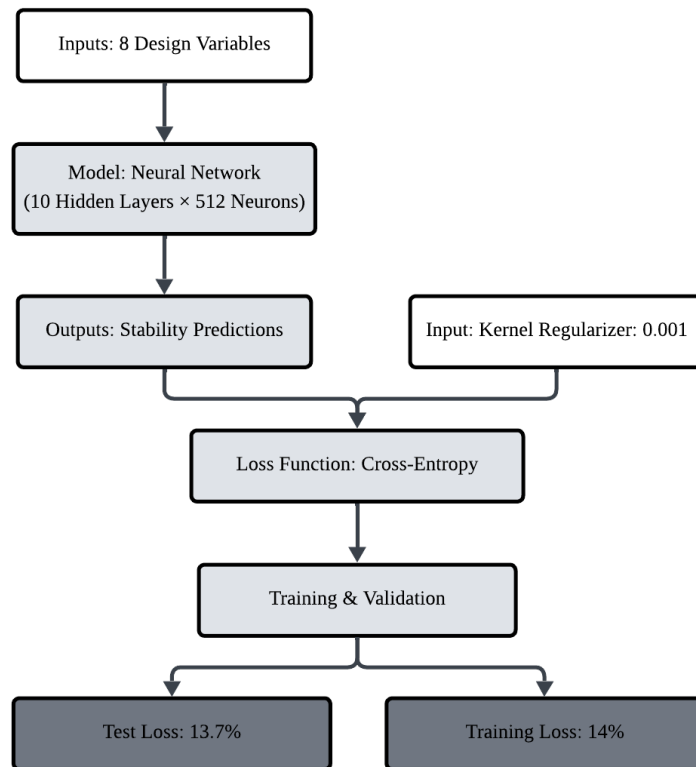


Fig. 6 Stability Neural Network process.

C. Optimized Wing Configurations (First Bounds)

This subsection presents the results of the optimized designs obtained from each solver mode (PSO, GA, gradient-based MultiStart, Bayesian, and Lipschitz). For each optimization method, we create space for four panels in a 2×2 arrangement: (1) planform comparison (initial vs. optimized), (2) lift/drag trajectories over iterations with the target lift line, (3) per-variable evolution curves for the eight design variables, and (4) coefficient histories CL/CD . All diagrams were created from the surrogate evaluations and optimization logs.

For the optimization runs, initiation began by imposing boundaries for parameters that would produce a “normal” wing designs: lower boundaries of $[0.5, -3, 0, 1, 0, 0.2, -6, 35]$ and upper boundaries of $[1.4, 8, 7, 7.5, 5, 0.8, 6, 58]$. The parameters are, in order, root chord, angle-of-attack, sweep angle, half-span, twist angle, taper ratio, dihedral angle, and free-stream velocity. These limits resulted in plausible and reasonable ultralight aircraft wing geometries.

Figs. 7, 8, 9, 10, and 11 compare the five optimizers under identical design-variable bounds. The multi-start interior-point run (Fig. 7) takes small, targeted steps from the best sampled start and drives the lift constraint to nearly numerical equality, settling near a tapered, moderate-span planform. The two derivative-free global methods (Figs. 8 and 9) reduce drag more than the gradient-based solver while keeping the lift constraint within tolerance; both saturate the span bound and converge with smooth, monotone coefficient histories. Bayesian optimization (Fig. 10) tracks the lift target but accepts a slightly higher final drag, consistent with exploitation near the incumbent. The Lipschitz global search followed by local constrained polishing (Fig. 11) also achieves near-equality in lift after its final refinement step. Across all methods, the leveling off of per-variable traces and the CL/CD histories indicate convergence after a finite number of iterations.

The final designs in Table 6 highlight how each optimizer exploits different trade-offs. PSO and GA both push the span to its upper limit ($b = 7.50$ m) with low taper ($\lambda = 0.20$ for PSO, 0.33 for GA) and moderate incidence ($\alpha \approx 5.4\text{--}5.7^\circ$), while the gradient-based run favors a larger chord ($c_r = 1.04$ m), higher taper ($\lambda = 0.495$), slightly reduced span ($b = 7.28$ m), and lower speed ($V = 42.7$ m/s). It also appears that the starting point of the method lies somewhere close to a local optimal solution since not many changes have been applied to the initial design point. Bayesian optimization instead selects the highest angle of attack (7.20°), the largest sweep ($\Lambda = 6.49^\circ$), and even a negative dihedral ($\Gamma = -1.30^\circ$) at the lowest speed ($V = 41.2$ m/s). Lipschitz optimization lands on a shorter span ($b = 5.88$ m) with mid-range taper ($\lambda = 0.391$) and intermediate speed ($V = 49.3$ m/s). The spread among these optima confirms that the search space is multimodal.

Aerodynamic metrics in Table 7 show that neural predictions agree closely with VLM recomputations: lift coefficients differ by less than 3% (worst case PSO at -2.63%), and drag predictions remain within 5% (worst case Lipschitz at -4.52%). Residuals in the lift constraint (ΔL) are modest (e.g., $+35$ N for Bayesian, -7.6 N for PSO), confirming the surrogate enforces the equality accurately.

Stability classifications in Table 8 further illustrate high consistency between the network and EoM, as the vast majority of derivatives are labeled consistently. The only systematic inconsistency is for the yaw-rate derivative N_R , where the network reports “semi-stable” sometimes, whereas the EoM model is classified as “unstable” (for Bayesian, GA, Lipschitz, and PSO). The gradient-based optimum yields total consistency on N_R (both stable), due to its smoother geometry. In general, the criteria on stability of DoFs depend on the case and mission-specific design criteria; thus, the feasibility of the solutions relies on it as well.

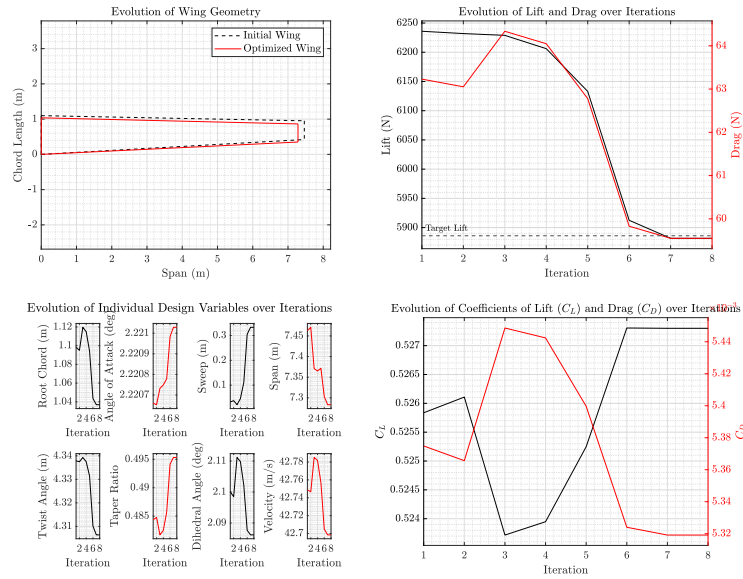


Fig. 7 Gradient-based (MultiStart + Interior points constrained optimization): optimized wing configuration and convergence diagnostics. Panels: (1) planform, (2) lift/drag, (3) design variables, (4) C_L and C_D .

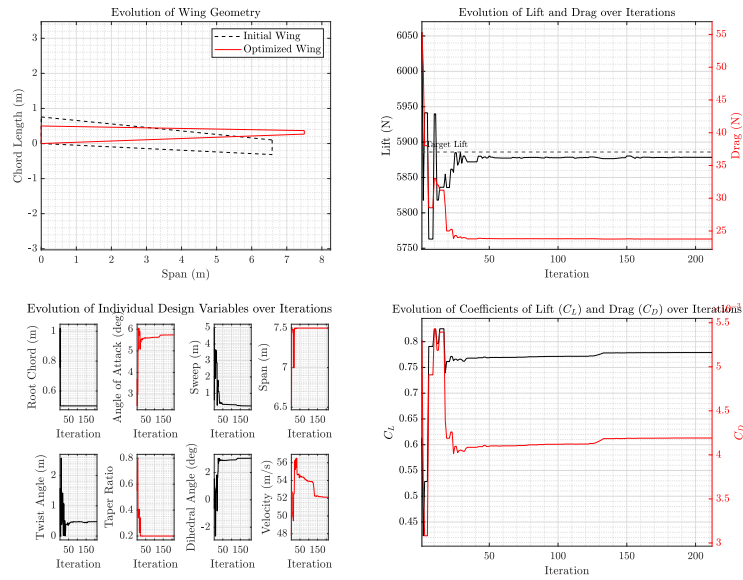


Fig. 8 Particle Swarm Optimization (PSO): optimized wing configuration and convergence diagnostics. Panels as in Fig. 7.

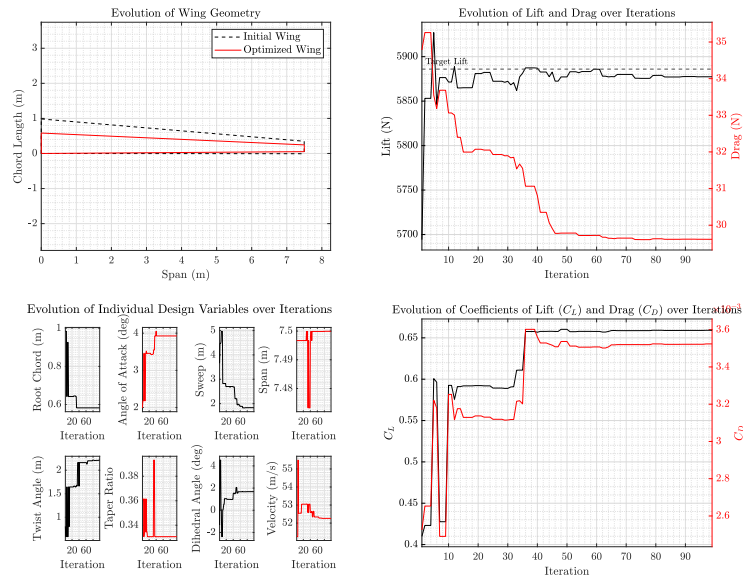


Fig. 9 Genetic Algorithm (GA): optimized wing configuration and convergence diagnostics. Panels as in Fig. 7.

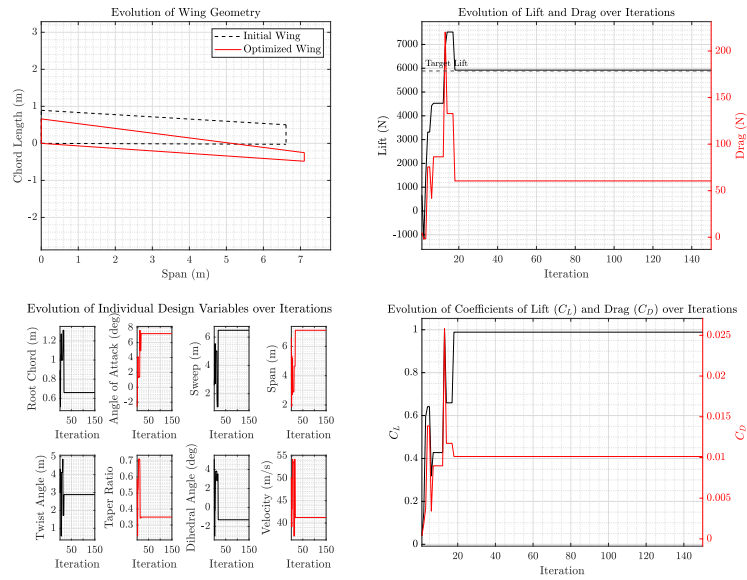


Fig. 10 Bayesian Optimization: optimized wing configuration and convergence diagnostics. Panels as in Fig. 7.

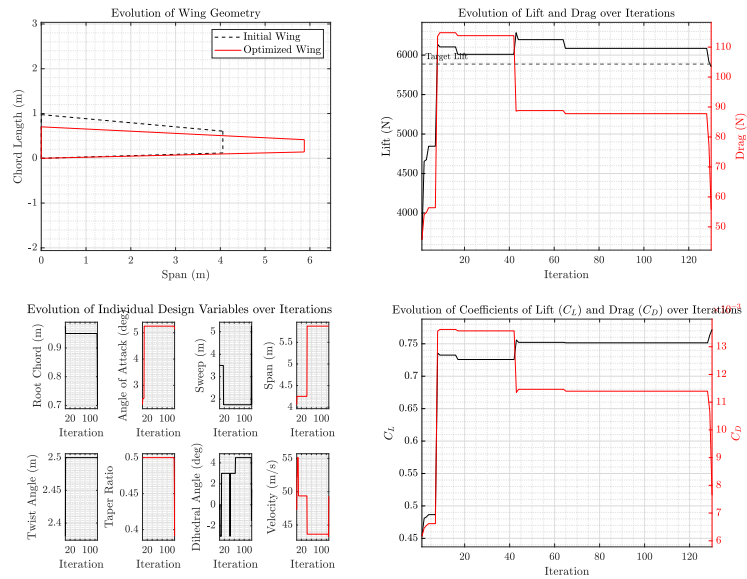


Fig. 11 Lipschitz optimization with adaptive L and local refinement: optimized wing configuration and convergence diagnostics. Panels as in Fig. 7.

Table 6 Final design variables using the first set of bounds. Symbols: c_r —root chord; α —angle of attack; Λ —quarter-chord sweep; b —wingspan; θ —twist; λ —taper ratio (c_t/c_r); Γ —dihedral; V —free-stream speed.

Method	c_r [m]	α [deg]	Λ [deg]	b [m]
	θ [deg]	λ	Γ [deg]	V [m/s]
Bayesian Optimization	6.61e-01	7.20e+00	6.49e+00	7.10e+00
	2.88e+00	3.50e-01	-1.30e+00	4.12e+01
Genetic Algorithm	5.82e-01	3.93e+00	1.83e+00	7.50e+00
	2.22e+00	3.31e-01	1.68e+00	5.23e+01
Gradient-Based Algorithm	1.04e+00	2.22e+00	3.33e-01	7.28e+00
	4.31e+00	4.95e-01	2.09e+00	4.27e+01
Lipschitz Optimization	7.03e-01	5.14e+00	1.75e+00	5.88e+00
	2.50e+00	3.91e-01	1.50e+00	4.93e+01
Particle Swarm Optimization	5.00e-01	5.74e+00	2.40e-01	7.50e+00
	4.74e-01	2.00e-01	3.04e+00	5.21e+01

Table 7 Aerodynamic metrics from NN and VLM using the first set of bounds. For NN: $\Delta L = L - L_{Constraint} = L - 600 \times 9.81$. Percentage differences are defined as $\% \Delta C_L = (C_{L_{NN}} - C_{L_{VLM}}) / C_{L_{VLM}}$ and $\% \Delta C_D = (C_{D_{NN}} - C_{D_{VLM}}) / C_{D_{VLM}}$.

Method	NN		VLM	
	C_L	C_D	C_L	C_D
	$\Delta L [N]$		$\% \Delta C_L$	$\% \Delta C_D$
Bayesian Optimization	9.89e-01	1.01e-02	9.89e-01	9.99e-03
	3.50e+01		-0.01%	1.21%
Genetic Algorithm	6.59e-01	3.52e-03	6.52e-01	3.68e-03
	-8.62e+00		1.03%	-4.15%
Gradient-Based Algorithm	5.27e-01	5.32e-03	5.29e-01	5.51e-03
	-4.37e+00		-0.35%	-3.54%
Lipschitz Optimization	7.72e-01	7.65e-03	7.64e-01	8.01e-03
	-3.22e+01		1.10%	-4.52%
Particle Swarm Optimization	7.79e-01	4.19e-03	8.00e-01	4.34e-03
	-7.56e+00		-2.63%	-3.40%

Table 8 Comparison of aerodynamic stability derivatives from NN and EoM using the first set of bounds. U = unstable, S = stable, SS = semi stable.

Method	F_{XU}	F_{YV}	M_α	N_β	M_Q
	M_U	F_{ZW}	L_β	L_P	N_R
Bayesian Optimization	NN: SS	U	S	U	SS
	EoM: SS	U	S	U	SS
	NN: SS	S	SS	S	SS
	EoM: SS	S	SS	S	U
Genetic Algorithm	NN: SS	U	S	S	SS
	EoM: SS	U	S	S	SS
	NN: SS	S	SS	S	SS
	EoM: SS	S	SS	S	U
Gradient-Based Algorithm	NN: SS	U	S	U	SS
	EoM: SS	U	S	U	SS
	NN: SS	S	SS	S	S
	EoM: SS	S	SS	S	S
Lipschitz Optimization	NN: SS	U	S	S	SS
	EoM: SS	U	S	S	SS
	NN: SS	S	SS	S	SS
	EoM: SS	S	SS	S	U
Particle Swarm Optimization	NN: SS	U	S	S	SS
	EoM: SS	U	S	S	SS
	NN: SS	S	SS	S	SS
	EoM: SS	S	SS	S	U

D. Different Bounds

To explore how the selection of the design domain ultimately influences the sensitivity of the optimization process, a second set of parameter bounds was applied: lower boundaries of [0.35, -3, 0, 4, 0, 0.1, 0, 35], upper boundaries of [1.3, 8, 7, 11, 5, 0.5, 6, 58]. This new set of limits gives longer and more slender, narrower wings, which are known to be better in terms of lower induced drag, but also have the potential for structural/stability issues; also, the wider parameter range requires the neural surrogates to extrapolate to the data mining boundaries, introducing further challenges to them in terms of potentially retrieving the underlying physics.

Figures 12, 13, 14, 15, and 16 illustrate the optimization workflow and dynamics for each method. The final optimized design variables are summarized in Table 9. The gradient-based method converged to a configuration next to the random starting point with a relatively large root chord ($c_r = 0.799$ m), small angle of attack ($\alpha = 1.46^\circ$), and long span ($b = 9.78$ m), combined with moderate taper ($\lambda = 0.252$) and free-stream velocity ($V = 56.8$ m/s). Lipschitz optimization produced a similar outcome with the gradient-based method showing that the final candidate solution point is near a local minimum with $c_r = 0.825$ m, $\alpha = 2.50^\circ$, and $b = 7.50$ m, but overshoot the lift constraint by about 53 N. In contrast, GA and PSO methods exploited the widened limits to push the span to the upper limit ($b \approx 11.0$ m) while keeping the root chord much smaller ($c_r = 0.373$ m for GA, $c_r = 0.350$ m for PSO), taper ratios near the lower bound ($\lambda = 0.159$ for GA, 0.100 for PSO), and moderate to high angles of attack ($\alpha = 5.36^\circ$ and 5.40°). These long and narrow wings produced particularly low drag while satisfying the lift equality within tolerance. Bayesian optimization converged to a mid-range solution with $c_r = 0.990$ m, $\alpha = 1.43^\circ$, $b = 8.74$ m, and $\lambda = 0.210$, balancing aerodynamic efficiency with adherence to constraints. Overall, the contrasting design trends confirm that the expanded bounds create a highly multi-modal landscape, where global optimizers (PSO, GA) tend toward extreme slender wings, while gradient-based and Bayesian approaches prefer intermediate geometries.

The aerodynamic metrics in Table 10 highlight the challenges faced by the surrogate when extrapolating beyond its training limits. For Bayesian optimization, the neural network predicted $C_L = 0.372$ and $C_D = 1.68 \times 10^{-3}$, compared to the VLM values of $C_L = 0.366$ and $C_D = 1.52 \times 10^{-3}$. This corresponds to a small C_L error (1.82%) but a significant C_D error of 10.56%. GA and PSO, while achieving very low drag levels, exhibit similarly large deviations: for PSO, the surrogate predicted $C_D = 2.48 \times 10^{-3}$ versus VLM 2.06×10^{-3} (20.46% error), while GA yielded $C_D = 2.22 \times 10^{-3}$ against 2.12×10^{-3} (4.75% error). Gradient-based optimization, though closer to the training region, still resulted in C_D deviations of nearly 10%. These results confirm that, unlike in the first-bound case, extrapolation under the expanded bounds substantially increases surrogate error.

The stability analysis in Table 11 shows that the surrogate do extrapolate reasonably well for most derivatives, consistently matching the EoM classification for F_{XU} , M_U , F_{YV} , F_{ZW} , M_α , L_β , and M_Q . However, the persistent misclassification issue for the yaw damping derivative N_R does remain: the surrogate often labeled it as semi-stable (SS) while the numerical linearization indicated unstable (U). This divergence is particularly evident across GA, PSO,

and Bayesian optimization runs, reflecting the difficulty of capturing the subtle boundary between semi-stable and unstable dynamics for this mode. Nonetheless, since not all derivatives need to be strictly stable for a feasible cruise condition, the optimized designs can be considered valid.

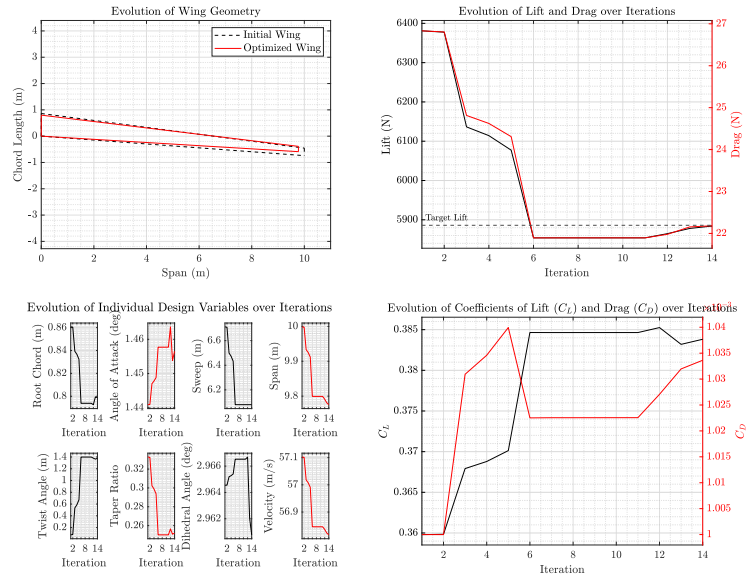


Fig. 12 Gradient-based optimization (different bounds): results shown in the same format as Fig. 7.

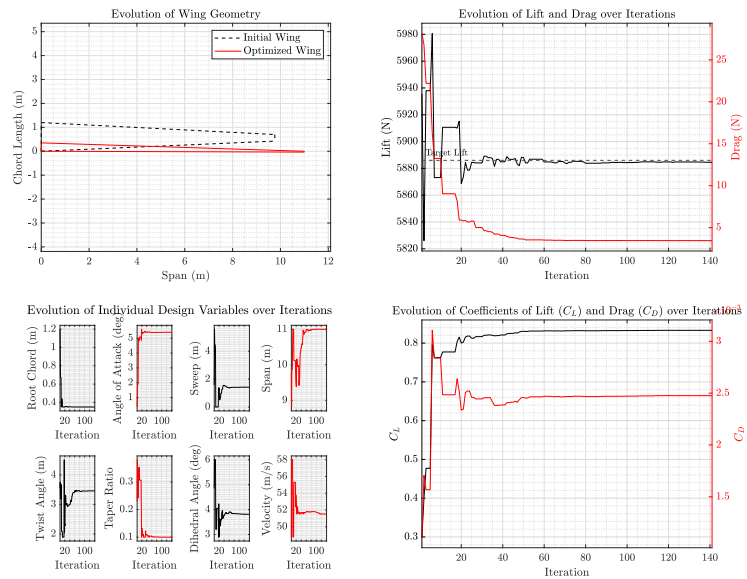


Fig. 13 Particle Swarm Optimization (different bounds): results shown in the same format as Fig. 8.

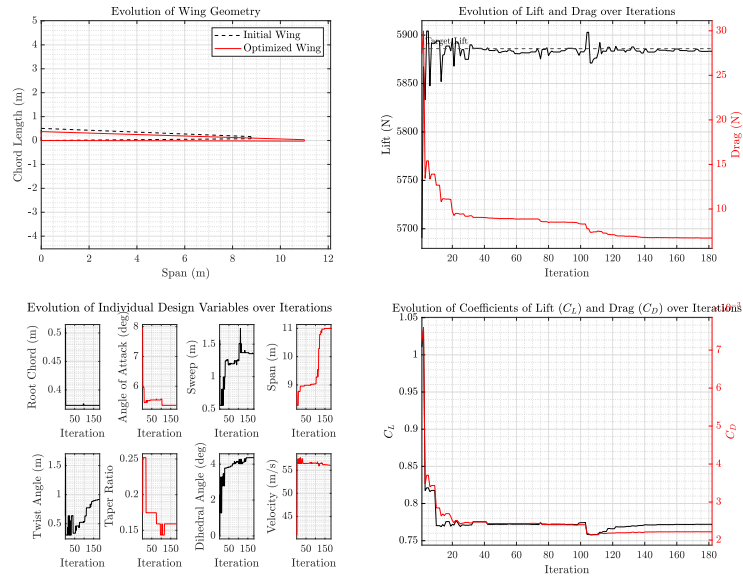


Fig. 14 Genetic Algorithm (different bounds): results shown in the same format as Fig. 9.

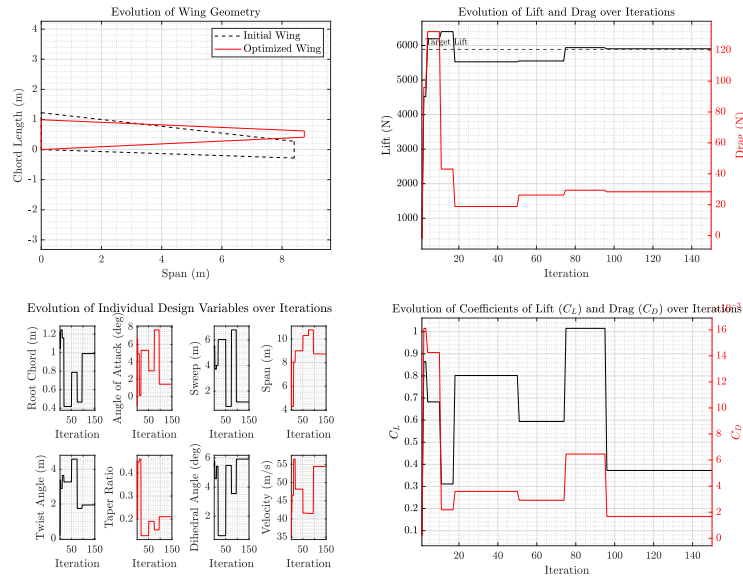


Fig. 15 Bayesian Optimization (different bounds): results shown in the same format as Fig. 10.

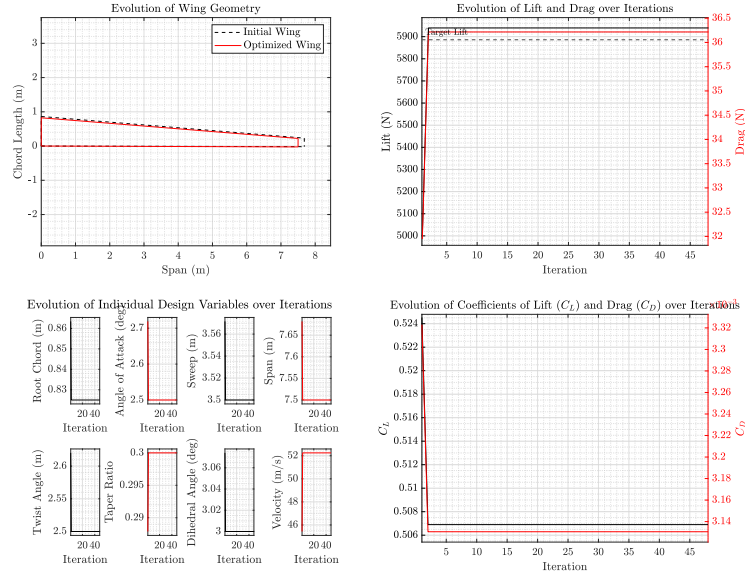


Fig. 16 Lipschitz optimization (different bounds): results shown in the same format as Fig. 11.

Table 9 Final design variables using the second set of bounds. Symbols: c_r —root chord; α —angle of attack; Λ —quarter-chord sweep; b —wingspan; θ —twist; λ —taper ratio (c_t/c_r); Γ —dihedral; V —free-stream speed.

Method	c_r [m]	α [deg]	Λ [deg]	b [m]
	θ [deg]	λ	Γ [deg]	V [m/s]
Bayesian Optimization	9.90e-01	1.43e+00	1.15e+00	8.74e+00
	1.94e+00	2.10e-01	5.91e+00	5.45e+01
Genetic Algorithm	3.73e-01	5.36e+00	1.35e+00	1.10e+01
	9.15e-01	1.59e-01	4.36e+00	5.61e+01
Gradient-Based Algorithm	7.99e-01	1.46e+00	6.08e+00	9.78e+00
	1.38e+00	2.52e-01	2.96e+00	5.68e+01
Lipschitz Optimization	8.25e-01	2.50e+00	3.50e+00	7.50e+00
	2.50e+00	3.00e-01	3.00e+00	5.23e+01
Particle Swarm Optimization	3.50e-01	5.40e+00	1.42e+00	1.10e+01
	3.46e+00	1.00e-01	3.81e+00	5.15e+01

Table 10 Aerodynamic metrics from NN and VLM using the second set of bounds. For NN: $\Delta L = L - L_{Constraint} = L - 600 \times 9.81$. Percentage differences are defined as $\% \Delta C_L = (C_{L_{NN}} - C_{L_{VLM}}) / C_{L_{VLM}}$ and $\% \Delta C_D = (C_{D_{NN}} - C_{D_{VLM}}) / C_{D_{VLM}}$.

Method	NN		VLM	
	C_L $\Delta L [N]$	C_D	C_L $\% \Delta C_L$	C_D $\% \Delta C_D$
Bayesian Optimization	3.72e-01	1.68e-03	3.66e-01	1.52e-03
	1.93e+01		1.82%	10.56%
Genetic Algorithm	7.72e-01	2.22e-03	7.81e-01	2.12e-03
	-2.66e+00		-1.20%	4.75%
Gradient-Based Algorithm	3.84e-01	1.03e-03	3.69e-01	1.15e-03
	-1.96e+00		3.91%	-9.94%
Lipschitz Optimization	5.07e-01	3.13e-03	4.97e-01	2.94e-03
	5.34e+01		1.97%	6.61%
Particle Swarm Optimization	8.33e-01	2.48e-03	8.08e-01	2.06e-03
	-1.42e+00		3.06%	20.46%

Table 11 Comparison of aerodynamic stability derivatives from NN and EoM using the second set of bounds. U = unstable, S = stable, SS = semi stable.

Method	F_{XU}	F_{YV}	M_α	N_β	M_Q
	M_U	F_{ZW}	L_β	L_P	N_R
Bayesian Optimization	NN: SS	U	S	U	SS
	EoM: SS	U	S	U	SS
	NN: SS	S	SS	S	S
	EoM: SS	S	SS	S	S
Genetic Algorithm	NN: SS	U	S	S	SS
	EoM: SS	U	S	S	SS
	NN: SS	S	SS	S	SS
	EoM: SS	S	SS	S	U
Gradient-Based Algorithm	NN: SS	U	S	U	SS
	EoM: SS	U	S	U	SS
	NN: SS	S	SS	S	S
	EoM: SS	S	SS	S	S
Lipschitz Optimization	NN: SS	U	S	U	SS
	EoM: SS	U	S	U	SS
	NN: SS	S	SS	S	S
	EoM: SS	S	SS	S	S
Particle Swarm Optimization	NN: SS	U	S	S	SS
	EoM: SS	U	S	S	SS
	NN: SS	S	SS	S	SS
	EoM: SS	S	SS	S	U

V. Discussion, Limitations, and Future Work

The CHIMERA framework illustrates the benefit of integrating surrogate modeling with an ensemble of optimization methods to accelerate and improve the wing design process. Across the solvers employed, particle swarm optimization (PSO) and genetic algorithms (GA) consistently provided the lowest drag while fulfilling the lift constraints; these employed solvers were particularly robust in multimodal search spaces. Lipschitz and Bayesian optimization produced the most conservative results, while optimization using the interior-point method produced smoother geometries, satisfying all constraints. The performance differences of all solvers highlight the distinct trade-off between exploration, exploitation, and handling of constraints by each solver; therefore, an ensemble methodology was more paradigm over a single optimizer was advantageous.

Even though feasible designs were consistently generated, the ensemble highlighted that the accuracy of the surrogate was sensitive to the coverage of the training data in the domain of interest. Drifting drag and lift predictions occurred when extrapolation was applied outside of the sampling domain, demonstrating the risks of approximating nonlinear aerodynamic characteristics using a finite dataset. Furthermore, stability modeling added an additional layer of complexity; the stability network was only used for feasibility filtering. Had we included the stability derivatives into the optimization objective, we could improve the tradeoff between performance and robustness, although this requires an improved training strategy and explicit multi-objective formulation.

The evaluation of ultralight glider wings under the strict assumptions of steady, incompressible flow limits the generalizability of the framework. The effects of compressibility, structural elasticity, and control surface deflection were considered to be negligible, and tail geometry was completely fixed, as the tail was not modeled within the Vortex Lattice Method (VLM) solver, leading to tail aerodynamic interactions being neglected as well. Future implementations could allow for the tail to be treated explicitly as a design variable to be optimized alongside the wing, allowing for the coupled effects to be captured more accurately.

The research findings indicate broader difficulties with surrogate-assisted aero-optimization. Data-driven models still heavily rely on the coverage and quality of the training datasets, stability predictions are less mature than aerodynamic predictions, and global optimization methods provide greater stability against multi-modality but are computationally demanding. As a result, although surrogate-driven ensembles reduce reliance on expensive high-fidelity solvers, they also introduce another set of complexities that need to be considered with caution during analysis.

We outline four specific approaches for transforming CHIMERA from a research prototype to a generalized design tool:

- 1) **Data enrichment and multi-fidelity modeling:** Combine low- and high-fidelity solvers (e.g., VLM + RANS/LES) with transfer learning to mitigate surrogate errors and improve accuracy under distribution shift.
- 2) **Stability-aware optimization:** Embed stability derivatives directly into the objective and/or adopt multi-objective formulations that co-optimize aerodynamic performance and dynamic robustness, replacing the current feasibility-

only filter.

- 3) **Expanded physics and actuation:** Incorporate compressibility effects, structural flexibility (aeroelastic coupling), and control effectiveness (deflections, hinge moments) to broaden applicability beyond steady, incompressible assumptions.
- 4) **Explicit tail integration:** Extend the VLM modeling to include tail geometry as design variables, enabling joint wing–tail optimization and capturing interaction effects during trim and stability analysis.

Progressing along these directions should, in theory, improve surrogate fidelity, guarantee stability, and increase the reliability and scope of the optimization ensemble to ultimately increase the practicality of CHIMERA for real-world aerospace design workflows.

VI. Conclusions

This paper showcased a pipeline that combines aerodynamic simulation based on vortex-lattice, surrogate neural networks, and multiple optimization methods in an integrated design framework. The methodology was implemented for the conceptual design of ultralight glider wings, illustrating that surrogate-driven optimization can significantly accelerate the design cycle.

Among the studied algorithms, Particle Swarm Optimization (PSO) and Genetic Algorithms (GA) consistently produced better aerodynamic performance, balancing global search capabilities to identify low-drag configurations within the feasible design space. Gradient-based and Bayesian methods produced solutions that are typically more conservative; however, they also provided smooth and constraint-adherent solutions, demonstrating the optimization paradigm’s different and complementary strengths. This demonstrates the benefits of a multi-method ensemble approach, where multiple algorithms allow for a more complete examination of the design space.

Implementing dual neural-network surrogates enabled efficient evaluation of aerodynamic loads and stability characteristics without having to rely on significantly more expensive solvers. Although in most instances, the predictions of the surrogate were nearly the same as the reference VLM computations, there were challenges in extrapolating and in stability derivative classifications. The results indicate the need for a careful dataset design in the future, as well as potential interest in stability-aware surrogate refinements.

Overall, CHIMERA represents a compelling and extensible platform for surrogate-assisted aero-optimization. The current implementation is focused on ultralight glider preliminary design stages; however, the modularity of the framework allows future enhancements to be made toward higher-fidelity aerodynamics, multi-disciplinary optimization, and across broader classes of aircraft. Lastly, by publicly releasing the full implementation, this research provides a reproducible and adaptable tool for the community in aerospace, supporting ongoing efforts in investigating data-driven and hybrid optimization methodologies.

A. Equations of Motion and Stability

This appendix summarizes the kinematics, aerodynamic load formulation, rigid-body dynamics, and the linear stability derivatives employed in the analysis of fixed-wing aircraft. All formulas in this appendix are drawn from [43]. Conventions: body axes (x, y, z) point forward, right, and down; angular rates (p, q, r) are positive about (x, y, z) ; gravity $g > 0$ acts downward. Moments are taken about the center of gravity (CG). Aerodynamic coefficients are referenced to (S, b, c) ; unless noted, the aerodynamic moment reference is at the quarter-chord.

A. Frames, angles, and dynamic pressure

Let the body-axis velocity be $v_b = [U, V, W]^T$. The airspeed and dynamic pressure are

$$\mathcal{V} = \sqrt{U^2 + V^2 + W^2}, \quad q = \frac{1}{2}\rho \mathcal{V}^2. \quad (1)$$

Angle of attack α and sideslip β define the conventional rotations. The body-to-stability transformation (rotation about body y by α) is

$$C_{sb}(\alpha) = \begin{bmatrix} \cos \alpha & 0 & \sin \alpha \\ 0 & 1 & 0 \\ -\sin \alpha & 0 & \cos \alpha \end{bmatrix}, \quad C_{bs} = C_{sb}^T, \quad (2)$$

and the body-to-wind transformation (rotation about y by α , then about z by β) is

$$C_{wb}(\alpha, \beta) = \begin{bmatrix} \cos \beta \cos \alpha & \sin \beta & \cos \beta \sin \alpha \\ -\sin \beta \cos \alpha & \cos \beta & -\sin \beta \sin \alpha \\ -\sin \alpha & 0 & \cos \alpha \end{bmatrix}. \quad (3)$$

B. Aerodynamic coefficients and dimensional loads

Let (S, b, c) indicate reference area, reference span, and mean aerodynamic chord, respectively. The dimensional loads in a chosen output frame (body, stability, or wind axes) are determined by the aerodynamic coefficients:

$$\begin{bmatrix} X \\ Y \\ Z \end{bmatrix} = q S \begin{bmatrix} C_X \\ C_Y \\ C_Z \end{bmatrix}, \quad \begin{bmatrix} L \\ M \\ N \end{bmatrix} = q S \begin{bmatrix} b C_\ell \\ c C_m \\ b C_n \end{bmatrix}. \quad (4)$$

The contributions from the airframe, control surfaces, and propulsion are additive. The linear parameterization used in the analysis is:

$$\begin{aligned}
C_m &\supset C_{m_\alpha} \alpha + C_{m_q} q + C_{m_{\delta_e}} \delta_e + \dots, \\
C_Y &\supset C_{Y_\beta} \beta + C_{Y_p} p + C_{Y_r} r + C_{Y_{\delta_a}} \delta_a + C_{Y_{\delta_r}} \delta_r + \dots, \\
C_X &\supset C_{X_U} U + C_{X_\alpha} \alpha + C_{X_{\delta_T}} \delta_T + \dots,
\end{aligned} \tag{5}$$

with analogous terms for C_Z, C_ℓ, C_n .

C. Six-degree-of-freedom rigid-body dynamics

With mass m , body rates $\omega_b = [p, q, r]^\top$, inertia tensor I , and gravity resolved in body axes g_b , the Newton–Euler equations are

$$m \dot{v}_b = \begin{bmatrix} X \\ Y \\ Z \end{bmatrix} - \omega_b \times (m v_b) + m g_b, \quad I \dot{\omega}_b + \omega_b \times (I \omega_b) = \begin{bmatrix} L \\ M \\ N \end{bmatrix}. \tag{6}$$

Using 3–2–1 (yaw–pitch–roll) Euler angles (ϕ, θ, ψ) , the attitude kinematics are

$$\begin{bmatrix} \dot{\phi} \\ \dot{\theta} \\ \dot{\psi} \end{bmatrix} = \begin{bmatrix} 1 & \sin \phi \tan \theta & \cos \phi \tan \theta \\ 0 & \cos \phi & -\sin \phi \\ 0 & \sin \phi \sec \theta & \cos \phi \sec \theta \end{bmatrix} \begin{bmatrix} p \\ q \\ r \end{bmatrix}. \tag{7}$$

D. Linearization and derivative notation

Let overbars denote trim values and lowercase denote perturbations (e.g., $U = \bar{U} + u$, $p = \bar{p} + \tilde{p}$, etc.). Around a steady trim (\bar{x}, \bar{u}) , partial derivatives of the load maps with respect to state variables are

$$\frac{\partial}{\partial \xi} \begin{bmatrix} X \\ Y \\ Z \\ L \\ M \\ N \end{bmatrix} = \begin{bmatrix} X_\xi \\ Y_\xi \\ Z_\xi \\ L_\xi \\ M_\xi \\ N_\xi \end{bmatrix}, \quad \xi \in \{U, V, W, \alpha, \beta, p, q, r\}. \tag{8}$$

The conventional groupings are

$$\text{Longitudinal: } \{X_U, X_W, X_q, X_\alpha; Z_U, Z_W, Z_q, Z_\alpha; M_U, M_W, M_q, M_\alpha\}, \quad (9)$$

$$\text{Lateral-Directional: } \{Y_V, Y_p, Y_r, Y_\beta; L_V, L_p, L_r, L_\beta; N_V, N_p, N_r, N_\beta\}. \quad (10)$$

E. Mapping from coefficient slopes to dimensional derivatives

Combining (4) with the linear parameterization yields

$$M_\alpha = qSc C_{m_\alpha}, \quad Y_\beta = qS C_{Y_\beta}, \quad L_p = qSb C_{\ell_p}, \quad M_q = qSc C_{m_q}, \quad N_r = qSb C_{n_r}, \quad \text{etc.} \quad (11)$$

When encoding rate dependencies against raw body rates, the common non-denationalization provides consistency:

$$C_{\ell_p} = \frac{b}{2V} \frac{\partial C_\ell}{\partial p}, \quad C_{m_q} = \frac{c}{2V} \frac{\partial C_m}{\partial q}, \quad C_{n_r} = \frac{b}{2V} \frac{\partial C_n}{\partial r}. \quad (12)$$

F. Dynamic-pressure coupling in X_U, Y_V, Z_W

Because $q = \frac{1}{2}\rho(U^2 + V^2 + W^2)$, derivatives with respect to (U, V, W) include both coefficient and dynamic-pressure dependence. At fixed ρ ,

$$X_U = S(q_U C_X + q C_{X,U}), \quad Y_V = S(q_V C_Y + q C_{Y,V}), \quad Z_W = S(q_W C_Z + q C_{Z,W}), \quad q_U = \rho U, \quad q_V = \rho V, \quad q_W = \rho W. \quad (13)$$

G. Control and propulsive derivatives

Let $\delta = \{\delta_e, \delta_a, \delta_r, \delta_T, \dots\}$ denote control and thrust settings. Linear control effects are defined by

$$\frac{\partial}{\partial \delta} \begin{bmatrix} X \\ Y \\ Z \\ L \\ M \\ N \end{bmatrix} = \begin{bmatrix} X_\delta \\ Y_\delta \\ Z_\delta \\ L_\delta \\ M_\delta \\ N_\delta \end{bmatrix}, \quad \begin{bmatrix} X_\delta \\ Y_\delta \\ Z_\delta \end{bmatrix} = qS \begin{bmatrix} C_{X,\delta} \\ C_{Y,\delta} \\ C_{Z,\delta} \end{bmatrix}, \quad \begin{bmatrix} L_\delta \\ M_\delta \\ N_\delta \end{bmatrix} = qS \begin{bmatrix} b C_{\ell,\delta} \\ c C_{m,\delta} \\ b C_{n,\delta} \end{bmatrix}. \quad (14)$$

Propulsive forces and moments (e.g., axial thrust) enter additively in X, Y, Z, L, M, N through their own $(\cdot)_\delta$ terms.

H. Static vs. dynamic stability sign tests

Under steady flight, the typical sign criteria are

$$\text{Static (force/angle slopes): } X_U < 0, Y_V < 0, Z_W < 0, M_\alpha < 0, L_\beta < 0, N_\beta > 0, \quad (15)$$

$$\text{Dynamic (rate damping): } M_q < 0, L_p < 0, N_r < 0. \quad (16)$$

Each derivative in (8) can be labeled *Stable*, *Unstable*, or *Neutral* according to these tests.

I. Canonical small-perturbation models

For trim ($\bar{\phi}, \bar{\theta}, \beta=0$), the linearized longitudinal and lateral-directional dynamics are

$$\begin{bmatrix} \dot{u} \\ \dot{w} \\ \dot{q} \\ \dot{\theta} \end{bmatrix} = \begin{bmatrix} X_u & X_w & X_q & -g \cos \bar{\theta} \\ Z_u & Z_w & Z_q & -g \sin \bar{\theta} \\ M_u & M_w & M_q & 0 \\ 0 & 0 & 1 & 0 \end{bmatrix} \begin{bmatrix} u \\ w \\ q \\ \theta \end{bmatrix} + \begin{bmatrix} X_{\delta_e} \\ Z_{\delta_e} \\ M_{\delta_e} \\ 0 \end{bmatrix} \delta_e + \dots, \quad (17)$$

$$\begin{bmatrix} \dot{v} \\ \dot{p} \\ \dot{r} \\ \dot{\phi} \\ \dot{\psi} \end{bmatrix} = \begin{bmatrix} Y_v & Y_p & Y_r & g \cos \bar{\theta} & 0 \\ L_v & L_p & L_r & 0 & 0 \\ N_v & N_p & N_r & 0 & 0 \\ 0 & 1 & \tan \bar{\theta} & 0 & 0 \\ 0 & 0 & \sec \bar{\theta} & 0 & 0 \end{bmatrix} \begin{bmatrix} v \\ p \\ r \\ \phi \\ \psi \end{bmatrix} + \begin{bmatrix} Y_{\delta_a} & Y_{\delta_r} \\ L_{\delta_a} & L_{\delta_r} \\ N_{\delta_a} & N_{\delta_r} \\ 0 & 0 \\ 0 & 0 \end{bmatrix} \begin{bmatrix} \delta_a \\ \delta_r \end{bmatrix} + \dots. \quad (18)$$

These canonical models provide the stability analysis, eigenmode identification, and control schemes.

B. Optimization Methods, Hyperparameters, & Pseudo Codes

We consider an 8-dimensional design vector $\mathbf{x} = [c_r, \alpha, \Lambda, b, \theta, \lambda, \Gamma, V]^\top$ subject to simple bounds $\mathbf{lb} \leq \mathbf{x} \leq \mathbf{ub}$ componentwise. Aerodynamic performance is predicted by a fixed surrogate

$$[L(\mathbf{x}), D(\mathbf{x})] = \mathcal{F}_{\text{aero}}(\mathbf{x}), \quad (1)$$

and stability is classified by

$$\mathbf{S}(\mathbf{x}) = \mathcal{F}_{\text{stab}}(\mathbf{x}). \quad (2)$$

A target-lift equality is imposed via

$$h(\mathbf{x}) \equiv \frac{600 \cdot 9.81}{L(\mathbf{x})} - 1 = 0, \quad (3)$$

i.e., $L(\mathbf{x}) = 600 \cdot 9.81$ N. Two scalar objectives are used:

$$f_g(\mathbf{x}) = \left(\frac{D(\mathbf{x})}{750} \right)^2, \quad \text{subject to } h(\mathbf{x}) = 0, \quad (4)$$

$$f_p(\mathbf{x}) = \left(\frac{D(\mathbf{x})}{100} \right)^2 + \rho \left(\frac{600 \cdot 9.81}{L(\mathbf{x})} - 1 \right)^2, \quad \rho = 100, \quad (5)$$

where (4) is minimized by the gradient-based method with the equality constraint (3), while (5) is used by the derivative-free global methods [44, 45]. All methods keep $\mathbf{lb} \leq \mathbf{x} \leq \mathbf{ub}$ at every step.

A. Gradient-based Method (Multi-start + Interior points)

This strategy solves the constrained problem

$$\min_{\mathbf{lb} \leq \mathbf{x} \leq \mathbf{ub}} f_g(\mathbf{x}) \quad \text{subject to } h(\mathbf{x}) = 0, \quad (6)$$

from multiple randomized starting points in the box $[\mathbf{lb}, \mathbf{ub}]$, returning the best feasible solution. Feasibility is understood as the simultaneous satisfaction of the simple bounds and the equality constraint within a numerical tolerance, i.e., $\mathbf{lb} \leq \mathbf{x} \leq \mathbf{ub}$ and $|h(\mathbf{x})| \leq 10^{-3}$.

The necessary optimality conditions at a local solution \mathbf{x}^* are the Karush–Kuhn–Tucker (KKT) conditions [46–48]. Let $\lambda \in \mathbb{R}$ be the multiplier of (3), and let $\alpha, \beta \in \mathbb{R}_{\geq 0}^8$ be the multipliers for the lower and upper bounds, respectively. Define the Lagrangian

$$\mathcal{L}(\mathbf{x}, \lambda, \alpha, \beta) = f_g(\mathbf{x}) + \lambda h(\mathbf{x}) + \alpha^\top (\mathbf{x} - \mathbf{lb}) - \beta^\top (\mathbf{x} - \mathbf{ub}). \quad (7)$$

Then a KKT point $(\mathbf{x}^*, \lambda^*, \boldsymbol{\alpha}^*, \boldsymbol{\beta}^*)$ satisfies

$$\nabla f_g(\mathbf{x}^*) + \lambda^* \nabla h(\mathbf{x}^*) + \boldsymbol{\alpha}^* - \boldsymbol{\beta}^* = \mathbf{0}, \quad (\text{stationarity}) \quad (8)$$

$$h(\mathbf{x}^*) = 0, \quad \mathbf{lb} \leq \mathbf{x}^* \leq \mathbf{ub}, \quad (\text{primal feasibility}) \quad (9)$$

$$\boldsymbol{\alpha}^* \geq \mathbf{0}, \quad \boldsymbol{\beta}^* \geq \mathbf{0}, \quad (\text{dual feasibility}) \quad (10)$$

$$\alpha_i^* (x_i^* - \text{lb}_i) = 0, \quad \beta_i^* (\text{ub}_i - x_i^*) = 0, \quad i = 1, \dots, 8, \quad (\text{complementarity}). \quad (11)$$

Under the Linear Independence Constraint Qualification and a second-order sufficiency condition (Lagrangian Hessian positive definite on the tangent space of active constraints), \mathbf{x}^* is a strict local minimizer of (6).

The end-to-end pipeline (import surrogates, multi-start launches, interior-point enforcement, and stability classification) is summarized in Table 12; the hyperparameters are listed in Table 13.

Table 12 Pipeline (pseudocode) for Gradient-based Method (Multi-start + Interior points)

Pseudocode

1. Import $\mathcal{F}_{\text{aero}}$, $\mathcal{F}_{\text{stab}}$, and scaling.
 2. Draw n_{starts} initial points uniformly in $[\mathbf{lb}, \mathbf{ub}]$.
 3. For each start: solve (6) with an interior-point method; store the feasible solution trajectory.
 4. Select the feasible solution with the smallest value of f_g .
 5. Evaluate stability: $\mathbf{S}(\mathbf{x}^*) = \mathcal{F}_{\text{stab}}(\mathbf{x}^*)$; report any unstable DOFs.
-

Table 13 Hyperparameters for Gradient-based Method (Multi-start + Interior points)

Number of starts	20
Objective	f_g in (4)
Nonlinear equality	$h(\mathbf{x}) = 0$ in (3)
Max iterations (inner solver)	5000
Max function evaluations	10^6
Step tolerance	10^{-12}
Optimality tolerance	10^{-6}
Constraint tolerance	10^{-3}
Bounds	$\mathbf{lb} \leq \mathbf{x} \leq \mathbf{ub}$

B. Particle Swarm Optimization (PSO)

In PSO, particle velocities and positions evolve according to

$$\mathbf{v}^+ = W \mathbf{v} + c_1 \mathbf{u}_1 \odot (\mathbf{p} - \mathbf{x}) + c_2 \mathbf{u}_2 \odot (\mathbf{g} - \mathbf{x}), \quad (12)$$

$$\mathbf{x}^+ = \Pi_{[\mathbf{lb}, \mathbf{ub}]}(\mathbf{x} + \mathbf{v}^+), \quad (13)$$

where W is the inertia, c_1, c_2 are cognitive/social weights, $\mathbf{u}_1, \mathbf{u}_2 \sim \mathcal{U}[0, 1]^8$ act componentwise, \mathbf{p} is the particle best, and \mathbf{g} is the swarm best. PSO minimizes the penalized objective f_p in (5). Classical PSO and its convergence analysis follow [49, 50]. The full PSO pipeline and hyperparameters appear in Tables 14 and 15, respectively.

Table 14 Pipeline (pseudocode) for PSO

Pseudocode

1. Import $\mathcal{F}_{\text{aero}}, \mathcal{F}_{\text{stab}}$, and scaling.
 2. Initialize positions in $[\mathbf{lb}, \mathbf{ub}]$ and velocities.
 3. Iterate: evaluate $[L, D] = \mathcal{F}_{\text{aero}}(\mathbf{x})$, compute h and f_p ; update personal and global bests; update (12)–(13); record best design.
 4. Terminate on stall/iteration limits; return best penalized design \mathbf{x}^* .
 5. Stability check: $\mathbf{S}(\mathbf{x}^*)$ from $\mathcal{F}_{\text{stab}}$; report instabilities.
-

Table 15 Hyperparameters for PSO

Swarm size	200
Max iterations	1000
Max stall iterations	20
Cognitive/social weights	1.49
Objective	f_p in (5)
Penalty magnitude	$\rho = 100$
Bounds	$\mathbf{lb} \leq \mathbf{x} \leq \mathbf{ub}$

C. Genetic Algorithm (GA)

The GA operates on a population using fitness proportional to $-f_p$. Parents are selected (e.g., stochastic uniform), recombined by convex or heuristic crossover, and mutated by random perturbations, with each offspring projected back to the box $[\mathbf{lb}, \mathbf{ub}]$. This method minimizes the penalized objective f_p in (5). Foundational references include Holland [51] and Goldberg [52]. The end-to-end pipeline and hyperparameters are shown in Tables 16 and 17.

Table 16 Pipeline (pseudocode) for GA

Pseudocode

1. Import $\mathcal{F}_{\text{aero}}, \mathcal{F}_{\text{stab}}$, and scaling.
 2. Initialize a population in $[\mathbf{lb}, \mathbf{ub}]$.
 3. For each generation: evaluate f_p ; select parents; apply crossover and mutation; project offspring to $[\mathbf{lb}, \mathbf{ub}]$; record incumbent.
 4. Stop on stall/generation limit; return best penalized design \mathbf{x}^* .
 5. Stability check: $\mathbf{S}(\mathbf{x}^*)$ from $\mathcal{F}_{\text{stab}}$.
-

Table 17 Hyperparameters for GA

Population size	200
Max generations	1000
Max stall generations	20
Objective	f_p in (5)
Penalty magnitude	$\rho = 100$
Bounds	$\mathbf{lb} \leq \mathbf{x} \leq \mathbf{ub}$

D. Bayesian Optimization

Bayesian optimization fits a surrogate g_t to observed pairs $\mathcal{D}_t = \{(\mathbf{x}_i, y_i)\}_{i=1}^t$, where $y_i = f_p(\mathbf{x}_i)$, and selects the next point by maximizing an acquisition function over the box $[\mathbf{lb}, \mathbf{ub}]$. Using expected improvement (EI), the acquisition is

$$EI_t(\mathbf{x}) = (f_{\min} - \mu_t(\mathbf{x})) \Phi\left(\frac{f_{\min} - \mu_t(\mathbf{x})}{\sigma_t(\mathbf{x})}\right) + \sigma_t(\mathbf{x}) \phi\left(\frac{f_{\min} - \mu_t(\mathbf{x})}{\sigma_t(\mathbf{x})}\right), \quad (14)$$

where $\mu_t(\mathbf{x})$ and $\sigma_t(\mathbf{x})$ are the surrogate posterior mean and standard deviation, and f_{\min} is the incumbent objective value. The pipeline and hyperparameters are in Tables 18 and 19. This lineage follows Kushner [53] and Mockus et al. [54], with the modern EGO formulation of Jones et al. [55].

Table 18 Pipeline (pseudocode) for Bayesian optimization**Pseudocode**

1. Import $\mathcal{F}_{\text{aero}}$, $\mathcal{F}_{\text{stab}}$, and scaling.
2. Define 8 optimizable variables on $[\mathbf{lb}, \mathbf{ub}]$; draw N_{seed} points; evaluate f_p .
3. Iterate: fit/update surrogate; select \mathbf{x}_{t+1} by maximizing EI (14); evaluate $f_p(\mathbf{x}_{t+1})$.
4. Return the best penalized design \mathbf{x}^* found.
5. Stability check: $\mathbf{S}(\mathbf{x}^*)$ from $\mathcal{F}_{\text{stab}}$.

Table 19 Hyperparameters for Bayesian optimization

Exploration ratio	0.8
Number of seed points	100
Max objective evaluations	150
Active set size (GP)	200
Objective	f_p in (5)
Penalty magnitude	$\rho = 100$
Bounds	$\mathbf{lb} \leq \mathbf{x} \leq \mathbf{ub}$

E. Lipschitz Global Search with Local Constrained Refinement

The global stage assumes f_p is L -Lipschitz on the box. The domain is partitioned into axis-aligned boxes $B \subset [\mathbf{lb}, \mathbf{ub}]$. For a box with center \mathbf{c}_B and diameter d_B (in ℓ_∞ norm), a characteristic lower-bound proxy is

$$\chi(B) = f_p(\mathbf{c}_B) - \widehat{L} \frac{d_B}{2}, \quad (15)$$

and boxes with smallest $\chi(B)$ are refined along their widest dimensions. The Lipschitz constant is estimated adaptively from all evaluated pairs via

$$\widehat{L} \leftarrow r \cdot \max_{i \neq j} \frac{|f_p(\mathbf{x}_i) - f_p(\mathbf{x}_j)|}{\|\mathbf{x}_i - \mathbf{x}_j\|_2}, \quad (16)$$

with reliability factor $r > 1$. When a selected box is sufficiently small, a local refinement solves the constrained problem (6) starting at the box center. The pipeline and hyperparameters are shown in Tables 20 and 21. See [56–58] for foundational Lipschitz global optimization.

Table 20 Pipeline (pseudocode) for Lipschitz global + local refinement

Pseudocode

1. Import $\mathcal{F}_{\text{aero}}$, $\mathcal{F}_{\text{stab}}$, and scaling.
 2. Initialize the full box $[\mathbf{lb}, \mathbf{ub}]$; evaluate f_p at its center; set a tiny initial \widehat{L} .
 3. Loop: update \widehat{L} by (16); compute $\chi(B)$ by (15);
 refine the smallest- χ box or stop on global tolerance;
 if local trigger met, solve (6) in that box to refine the incumbent.
 4. Return the best design \mathbf{x}^* ; evaluate $\mathbf{S}(\mathbf{x}^*)$ for stability.
-

Table 21 Hyperparameters for Lipschitz method

Global iteration budget	500
Global tolerance (box diameter)	10^{-3}
Local refinement trigger	6
Reliability factor r	1.1
Initial Lipschitz estimate	10^{-32}
Objective (global)	f_p in (5)
Objective (local)	f_g in (4) with $h(\mathbf{x}) = 0$
Bounds	$\mathbf{lb} \leq \mathbf{x} \leq \mathbf{ub}$

the Gradient-based method (Multi-start + Interior points) minimizes the constrained objective f_g in (4) while enforcing the equality (3). The three global derivative-free methods—PSO, GA, and Bayesian optimization—minimize the penalized objective f_p in (5). The Lipschitz strategy uses f_p for its global box selection via (15)–(16) and switches to the constrained objective f_g during the local refinement step. In all cases, the simple bounds $\mathbf{lb} \leq \mathbf{x} \leq \mathbf{ub}$ are maintained throughout.

References

- [1] He, S., Jonsson, E., Li, J., and Martins, J. R., “Adjoint-based design optimization of stability constrained systems,” *AIAA Journal*, Vol. 63, No. 3, 2025, pp. 1036–1048.
- [2] Li, J., and Zhang, M., “Adjoint-free aerodynamic shape optimization of the common research model wing,” *AIAA Journal*, Vol. 59, No. 6, 2021, pp. 1990–2000.
- [3] Abergo, L., Morelli, M., and Guardone, A., “Aerodynamic shape optimization based on discrete adjoint and RBF,” *Journal of Computational Physics*, Vol. 477, 2023, p. 111951.
- [4] Chen, W., Kou, J., Yang, W., and Pan, S., “Dynamic-mode-decomposition-based gradient prediction for adjoint-based aerodynamic shape optimization,” *Aerospace Science and Technology*, Vol. 150, 2024, p. 109175.
- [5] Khouzani, H. J., and Kamali-Moghadam, R., “Mathematical derivation of a unified equations for adjoint lattice Boltzmann method in airfoil and wing aerodynamic shape optimization,” *Communications in Nonlinear Science and Numerical Simulation*, Vol. 140, 2025, p. 108319.
- [6] Shi, Y., Lan, Q., Lan, X., Wu, J., Yang, T., and Wang, B., “Robust optimization design of a flying wing using adjoint and uncertainty-based aerodynamic optimization approach,” *Structural and Multidisciplinary Optimization*, Vol. 66, No. 5, 2023, p. 110.
- [7] Wu, H., Chen, R., Lou, J., You, Y., Huang, L., Xu, M., and Ruan, Y., “A gradient aerodynamic optimization method based on deep learning,” *Physics of Fluids*, Vol. 36, No. 5, 2024.
- [8] Hasan, M., Redonnet, S., and Zhongmin, D., “Aerodynamic optimization of aircraft wings using machine learning,” *Advances in Engineering Software*, Vol. 200, 2025, p. 103801.
- [9] Esfahanian, V., Izadi, M. J., Bashi, H., Ansari, M., Tavakoli, A., and Kordi, M., “Aerodynamic shape optimization of gas turbines: a deep learning surrogate model approach,” *Structural and Multidisciplinary Optimization*, Vol. 67, No. 1, 2024, p. 2.
- [10] Jabón, J., Corbera, S., Álvarez, R., and Barea, R., “Aerodynamic shape optimization using graph variational autoencoders and genetic algorithms,” *Structural and Multidisciplinary Optimization*, Vol. 67, No. 3, 2024, p. 32.
- [11] Wang, Y., Shimada, K., and Barati Farimani, A., “Airfoil GAN: Encoding and synthesizing airfoils for aerodynamic shape optimization,” *Journal of Computational Design and Engineering*, Vol. 10, No. 4, 2023, pp. 1350–1362.
- [12] Wu, M.-Y., Yuan, X.-Y., Chen, Z.-H., Wu, W.-T., Hua, Y., and Aubry, N., “Airfoil shape optimization using genetic algorithm coupled deep neural networks,” *Physics of Fluids*, Vol. 35, No. 8, 2023.
- [13] Zhang, Z., Ao, Y., Li, S., and Gu, G. X., “An adaptive machine learning-based optimization method in the aerodynamic analysis of a finite wing under various cruise conditions,” *Theoretical and Applied Mechanics Letters*, Vol. 14, No. 1, 2024, p. 100489.

- [14] Sabater, C., Stürmer, P., and Bekemeyer, P., “Fast predictions of aircraft aerodynamics using deep-learning techniques,” *AIAA Journal*, Vol. 60, No. 9, 2022, pp. 5249–5261.
- [15] Li, J., and Zhang, M., “On deep-learning-based geometric filtering in aerodynamic shape optimization,” *Aerospace Science and Technology*, Vol. 112, 2021, p. 106603.
- [16] Tao, G., Fan, C., Wang, W., Guo, W., and Cui, J., “Multi-fidelity deep learning for aerodynamic shape optimization using convolutional neural network,” *Physics of Fluids*, Vol. 36, No. 5, 2024.
- [17] Du, B., Shen, E., Wu, J., Guo, T., Lu, Z., and Zhou, D., “Aerodynamic Prediction and Design Optimization Using Multi-Fidelity Deep Neural Network.” *Aerospace (MDPI Publishing)*, Vol. 12, No. 4, 2025.
- [18] Nikolaou, E., Kilimtzidis, S., and Kostopoulos, V., “Multi-Fidelity Surrogate-Assisted Aerodynamic Optimization of Aircraft Wings,” *Aerospace*, Vol. 12, No. 4, 2025, p. 359.
- [19] Wu, M.-Y., He, X.-J., Sun, X.-H., Tong, T.-S., Chen, Z.-H., and Zheng, C., “Efficient aerodynamic shape optimization using transfer learning based multi-fidelity deep neural network,” *Physics of Fluids*, Vol. 36, No. 11, 2024.
- [20] Grbicic, L., Müller, J., and de Jong, W. A., “Efficient inverse design optimization through multi-fidelity simulations, machine learning, and boundary refinement strategies,” *Engineering with Computers*, Vol. 40, No. 6, 2024, pp. 4081–4108.
- [21] Matos, N. M., and Marta, A. C., “Aerodynamic Shape Optimization of Wing–Fuselage Intersection for Minimum Interference Drag,” *Aerospace*, Vol. 12, No. 5, 2025, p. 369.
- [22] Wang, K., Han, Z.-H., Zhang, K.-S., and Song, W.-P., “An efficient geometric constraint handling method for surrogate-based aerodynamic shape optimization,” *Engineering Applications of Computational Fluid Mechanics*, Vol. 17, No. 1, 2023, p. e2153173.
- [23] Deng, F., and Qin, N., “An exploitation-enhanced multi-objective efficient global optimization algorithm for expensive aerodynamic shape optimizations,” *Proceedings of the Institution of Mechanical Engineers, Part G: Journal of Aerospace Engineering*, Vol. 236, No. 7, 2022, pp. 1408–1421.
- [24] Li, Z., Wang, W., Xie, Y., and Li, D., “Optimization Design of Blades Based on Multi-Objective Particle Swarm Optimization Algorithm.” *Journal of Marine Science & Engineering*, Vol. 13, No. 3, 2025.
- [25] Bakar, A., Li, K., Liu, H., Xu, Z., Alessandrini, M., and Wen, D., “Multi-objective optimization of low reynolds number airfoil using convolutional neural network and non-dominated sorting genetic algorithm,” *Aerospace*, Vol. 9, No. 1, 2022, p. 35.
- [26] Asouti, V., Kontou, M., and Giannakoglou, K., “Radial basis function surrogates for uncertainty quantification and aerodynamic shape optimization under uncertainties,” *Fluids*, Vol. 8, No. 11, 2023, p. 292.
- [27] Jofre, L., and Doostan, A., “Rapid aerodynamic shape optimization under uncertainty using a stochastic gradient approach,” *Structural and Multidisciplinary Optimization*, Vol. 65, No. 7, 2022, p. 196.

- [28] Li, J., He, S., Martins, J. R., Zhang, M., and Cheong Khoo, B., "Efficient data-driven off-design constraint modeling for practical aerodynamic shape optimization," *AIAA Journal*, Vol. 61, No. 7, 2023, pp. 2854–2866.
- [29] Caros, L., Buxton, O., and Vincent, P., "Optimization of triangular airfoils for Martian helicopters using direct numerical simulations," *AIAA Journal*, Vol. 61, No. 11, 2023, pp. 4935–4945.
- [30] Hirooka, S., Kurahashi, T., Toyama, S., and Nonami, R., "Shape optimization of a corrugated wing to improve lift force," *JSIAM Letters*, Vol. 16, 2024, pp. 117–120.
- [31] Zhuang, X., Li, D., Wang, Y., Liu, X., and Li, H., "Optimization of high-speed fixed-wing UAV penetration strategy based on deep reinforcement learning," *Aerospace Science and Technology*, Vol. 148, 2024, p. 109089.
- [32] Luo, Z., Zhang, Y., Shi, Q., and Wang, X., "Aero-structural comprehensive nonprobabilistic reliability-based optimization method for high aspect ratio wings," *AIAA Journal*, Vol. 62, No. 11, 2024, pp. 4280–4291.
- [33] Li, P., "Hybrid Optimization for High Aspect Ratio Wings with Convolutional Neural Networks and Squirrel Optimization Algorithm," *Scalable Computing: Practice and Experience*, Vol. 25, No. 1, 2024, pp. 85–93.
- [34] Streuber, G. M., and Zingg, D. W., "Evaluating the risk of local optima in aerodynamic shape optimization," *AIAA Journal*, Vol. 59, No. 1, 2021, pp. 75–87.
- [35] Streuber, G. M., and Zingg, D. W., "Improved dynamic geometry control algorithms for efficient aerodynamic shape optimization," *AIAA Journal*, Vol. 61, No. 5, 2023, pp. 2116–2134.
- [36] Kedward, L. J., Allen, C. B., Poole, D. J., and Rendall, T. C., "Generic modal design variables for efficient aerodynamic optimization," *AIAA Journal*, Vol. 61, No. 2, 2023, pp. 739–755.
- [37] Li, J., and Zhang, M., "Data-based approach for wing shape design optimization," *Aerospace Science and Technology*, Vol. 112, 2021, p. 106639.
- [38] Chen, L., Rottmayer, J., Kusch, L., Gauger, N., and Ye, Y., "Data-driven aerodynamic shape design with distributionally robust optimization approaches," *Computer Methods in Applied Mechanics and Engineering*, Vol. 429, 2024, p. 117131.
- [39] Martins, J. R., "Aerodynamic design optimization: Challenges and perspectives," *Computers & Fluids*, Vol. 239, 2022, p. 105391.
- [40] He, Y., Hu, R., Liang, K., Liu, Y., and Zhou, Z., "Deep reinforcement learning algorithm with long short-term memory network for optimizing unmanned aerial vehicle information transmission," *Mathematics*, Vol. 13, No. 1, 2024, p. 46.
- [41] Hasan, M., and Khandoker, A., "Enhancing box-wing design efficiency through machine learning based optimization," *Chinese Journal of Aeronautics*, Vol. 38, No. 2, 2025, p. 103216.
- [42] Melin, T., "A vortex lattice MATLAB implementation for linear aerodynamic wing applications," *Royal Institute of Technology, Sweden*, Vol. 208, 2000.

- [43] Roskam, J., *Airplane design*, DARcorporation, 1997.
- [44] Bertsekas, D. P., *Constrained optimization and Lagrange multiplier methods*, Academic press, 2014.
- [45] Forrester, A., Sobester, A., and Keane, A., *Engineering design via surrogate modelling: a practical guide*, John Wiley & Sons, 2008.
- [46] Karush, W., “Minima of functions of several variables with inequalities as side conditions,” *Traces and emergence of nonlinear programming*, Springer, 2013, pp. 217–245.
- [47] Kuhn, H. W., and Tucker, A. W., “Nonlinear programming,” *Traces and emergence of nonlinear programming*, Springer, 2013, pp. 247–258.
- [48] Nocedal, J., and Wright, S. J., *Numerical optimization*, Springer, 2006.
- [49] Kennedy, J., and Eberhart, R., “Particle swarm optimization,” *Proceedings of ICNN’95-international conference on neural networks*, Vol. 4, iee, 1995, pp. 1942–1948.
- [50] Clerc, M., and Kennedy, J., “The particle swarm-explosion, stability, and convergence in a multidimensional complex space,” *IEEE transactions on Evolutionary Computation*, Vol. 6, No. 1, 2002, pp. 58–73.
- [51] Holland, J. H., *Adaptation in natural and artificial systems: an introductory analysis with applications to biology, control, and artificial intelligence*, MIT press, 1992.
- [52] Golberg, D. E., “Genetic algorithms in search, optimization, and machine learning,” *Addion wesley*, Vol. 1989, No. 102, 1989, p. 36.
- [53] Kushner, H. J., “A new method of locating the maximum point of an arbitrary multipeak curve in the presence of noise,” 1964.
- [54] Mockus, J., “The application of Bayesian methods for seeking the extremum,” *Towards global optimization*, Vol. 2, 1998, p. 117.
- [55] Jones, D. R., Schonlau, M., and Welch, W. J., “Efficient global optimization of expensive black-box functions,” *Journal of Global optimization*, Vol. 13, No. 4, 1998, pp. 455–492.
- [56] Piyavskii, S., “An algorithm for finding the absolute extremum of a function,” *USSR Computational Mathematics and Mathematical Physics*, Vol. 12, No. 4, 1972, pp. 57–67.
- [57] Shubert, B. O., “A sequential method seeking the global maximum of a function,” *SIAM Journal on Numerical Analysis*, Vol. 9, No. 3, 1972, pp. 379–388.
- [58] Horst, R., and Pardalos, P. M., *Handbook of global optimization*, Springer Science & Business Media, 2013.